On two-phase modelling of dewatering pulp suspensions

Daniel T. Paterson
Department of Chemical and Biological Engineering, University of British Columbia, Vancouver, BC, V6T 1Z4, Canada

Tom S. Eaves
School of Science and Engineering, University of Dundee, Fulton Building, Dundee, DD1 4HN, UK

Duncan R. Hewitt
Department of Mathematics, University College London, 25 Gordon Street, London, WC1H 0AY, UK

Neil J. Balmforth
Department of Mathematics, University of British Columbia, Vancouver, BC, V6T 1Z2, Canada

D. Mark Martinez
Department of Chemical and Biological Engineering, University of British Columbia, Vancouver, BC, V6T 1Z4, Canada

(Dated: August 18, 2020)

An experimental study of the dewatering of wood-pulp fibre suspensions by uniaxial compression is presented, to rationalise their dewatering dynamics within a two-phase framework. A variety of pulp suspensions are examined, encompassing materials with different origins, preparation methodologies, and secondary treatments. For each suspension in this library, the network permeability and compressive yield stress are calibrated at low rates of dewatering. Faster compressions are then used to verify that a solid bulk viscosity is essential to match two-phase model predictions with experimental observations, and to parametrize its magnitude. By comparing the results with a suspension of nylon fibres, we demonstrate that none of the wood-pulp suspensions behave like an idealized fibrous porous medium. Nevertheless, the properties of pulp fibre networks can be reconciled within a two-phase framework, and comparisons made between different wood-pulp suspensions and between wood-pulp and nylon fibres, by appealing to potential microstructural origins of their macroscopic behaviour.

Topical Heading: Transport Phenomena and Fluid Mechanics
Key Words: Suspensions – Solid/liquid separations – Porous media – Fibers – Multi-phase flow

I. INTRODUCTION

The dynamics of deformable porous media are central to a wide-range of problems in geophysics and biology and to a great many industrial processes. Consolidation or dewatering operations, for example, in which a significant volume of liquid is removed from a collapsing solid matrix, feature in sedimentology, the treatment of mine tailings and waste water, and the production of ceramics and paper products. Specific motivation for the current study stems from the pulp and paper industry where various operations surround the removal of water from suspensions of pulp fibres. In particular, the interrogation of these operations raises the question of whether such suspensions can be described as model, fibrous, deformable porous media. Indeed, discussions along these lines have been presented previously (*e.g.* [1–7]).

The two-phase description of deformable porous media (*e.g.* [8, 9]) typically identifies and focusses on two key material quantities: the permeability of the solid matrix and its ability to resist deformation, described by an effective solid stress. For a suspension of elongated deformable fibres, a solid matrix that resists stress can be established at volume fractions of less than a percent, but can also be compressed mechanically up to much higher concentrations with comparable volumes of fluid and solid. The permeability and solid stress must therefore span more than two orders of magnitude of solid fraction from the gel point of the material (defined by when the stress-supporting matrix is created) up to its maximum packing.

Classical treatments of permeability often describe its dependence on solid volume fraction in terms of the Carman-Kozeny law for a packed bed of curved passages or tubes. Jackson & James [10] comprehensively summarized

measurements and theories for a large range of different elongated, relatively rigid fibres, and concluded that these materials could also be conveniently described in terms of a suitably scaled permeability, independently of the fibrous material. However, suspensions of pulp fibres have repeatedly been found to be much less permeable in comparison to the Jackson-James scaling (*e.g.* [11–15]) raising questions about the network microstructure in pulp and whether these permeability measurements can be somehow shifted back into line.

The solid stress in a deformable suspension is typically taken to be elastic or plastic in origin. Either way, the stress is generally considered to be rate-independent and can be calibrated empirically as a function of the solid fraction to model the resistance to network collapse in response to significant deformations [8, 16–18]. Van Wyck [19] proposed a similar approach for fibre suspensions of wool and other textiles, assuming that collapse was resisted by the elastic bending of fibres (see also [20]), a prescription that was then partially repeated for wood pulp [21]. Van Wyck's scaling arguments suggest a certain volume-fraction dependence to the solid stress, borne out by experiments with a number of materials. Nevertheless, the same suspensions can display only limited recovery when unloading a previously compressed suspension, demonstrating that deformations cannot be entirely elastic (*e.g.* [22, 23]).

Pulp suspensions, in fact, often show very little recovery on unloading (*e.g.* [23–26]), indicating that the resistance is primarily plastic. Moreover, a number of recent studies have suggested that the solid stress must be rate-dependent in order to reproduce the observed dewatering and flow-induced compaction of pulp suspensions and capillary rise through paper sheets [15, 27, 28]. These studies have accounted for this rate-dependence by extending the description of the solid stress to include an effective bulk viscosity of the network, with some precedence existing in earlier work (*e.g.* [16, 26, 29–32]), or by analogy with the generic shear viscosity expected for a two-phase medium [33]. Thus, pulp suspensions appear to require an unconventional visco-plastic solid stress.

In detail, pulp suspensions are a mixture of wood fibres, water and clay, with small quantities of inorganic salts and polymeric additives. Wood fibres, the principle component, are hollow, flexible rod-like particles which have a wide distribution in length, diameter and morphology depending upon species, growing conditions, and method of liberation from the wood matrix. They are composed of three classes of biopolymers (cellulose, hemicellulose, and lignin) wound into a complex fibre-like substructure to create mechanical strength. Critically, morphological features such as pits allow fluid transport through the wall into the hollow interior, while water may also be imbibed into the ultrastructure of the wall itself. On grander scales of order millimetres, wood-fibres aggregate into coherent networks, through mechanical entanglement rather than by colloidal force, creating a complex three-dimensional architecture. The structure of the solid matrix in a typical pulp suspension is therefore significantly richer than that of a network of almost rigid circular cylinders (Jackson & James's idealized fibrous medium). In addition, during the pre-processing leading to papermaking, the fibres are typically chemically-functionalized or mechanically-beaten, altering the chemical composition, surface charge or morphological features in order to adjust or control the dewatering behaviour and properties of the final product. Given such complications, it is perhaps not surprising that pulp suspensions display what appears to be non-ideal behaviour.

The aim of the present study is to record and rationalize this non-ideal behaviour for a large suite of different pulp suspensions, and to demonstrate how pulp suspensions appear to fall into a new two-phase-model paradigm. More specifically, after introducing the two-phase modelling framework, we explore experimentally the dewatering behaviour of a wide variety of different pulp-fibre suspensions. This 'library' of pulp suspensions encompasses some of the microstructural variability encountered in the papermaking industry by combining fibres with different wood origins and means of preparation and treatment. For the library of suspensions, we first calibrate the two traditional material quantities that characterize deformable porous media (permeability and compressive solid stress) at relatively low rates of compaction. We then conduct compressive dewatering tests at different rates of compaction in order to gauge whether a rate-dependence is required in the solid stress, and if so, to calibrate its magnitude for each pulp. We further interrogate the library to gauge whether we can detect the impact of any microstructural differences on the macroscopic material behaviour. Throughout, we compare with scaling theories based on idealized descriptions of microstructural deformation and flow to judge if a relatively simple physical picture might underscore our observations.

II. MATERIALS, MODELLING AND METHODS

A. Materials

Twenty-seven fibre suspensions are assembled into our pulp library to give some representation of the variability encountered in papermaking processes due to differences in fibre origin, pulping methodology, energy level during mechanical beating (known as LC refining or LCR), and polymer additives. Table I lists details of the pulps, which are derived from a number of commercially available fibres. In particular, the table provides a brief description of the type of pulp, the pulping method used in its production, and whether polymeric additives or LC refining was used for further treatments. These details are complemented with the mean length L and width W, measured in an Optest

TABLE I: A table of pulp suspensions used for the library, showing the series reference number, the symbol used to plot experimental data, the line style used for fits of permeability and compressive yield stress, the wood origin and pulping methodology, any chemical additives, the degree of mechanical refining, the Canadian Standard Freeness score (CSF), and the mean fibre length L and width W.

Series	Symbol	Line	Description			Details		
			Material	Additive	LCR [kWh/t]	CSF [mL]	L [mm]	W [μm]
1[a]	△	——	NBSK (Canfor)[b]			705	2.57	26.7
2	■	——	NBSK (SCA, Östrand)[c]			680	2.15	25.5
3	□	——	SBK (Resolute, Catawba)[d]			730	2.45	26.8
4[a]	●	——	HBK (Domtar)[e]			610	0.79	20.1
5	▲	——	HBK (Fibria)[f]			415	0.76	16.2
6	×	——	HBK (Fibria) 80%	NBSK (Canfor) 20%		480	0.95	16.6
7	●	— — —	HBK (Fibria) 60%	NBSK (Canfor) 40%		530	1.16	17.3
8	▲	· · · · · ·	HBK (Fibria) 40%	NBSK (Canfor) 60%		575	1.46	18.2
9	■	— · — · —	HBK (Fibria) 20%	NBSK (Canfor) 80%		635	1.83	20.3
10	+	——	NBSK (Canfor)	Polymer 1[j]		705	2.57	26.7
11[a]	×	— — —	NBSK (Canfor)	Polymer 2[k]		745	2.57	26.7
12[a]	□	· · · · · ·	NBSK (Canfor)	Polymer 3[l]		760	2.57	26.7
13	◊	— · — · —	NBSK (Canfor)	Polymer 4[m]		710	2.57	26.7
14	◯	—— —— ——	NBSK (Canfor)	Polymer 5[n]		720	2.57	26.7
15	■	— — —	NBSK (Canfor)		47	500	2.60	26.9
16	♦	· · · · · ·	NBSK (Canfor)		95	385	2.59	27.0
17	▲	— · — · —	NBSK (Canfor)		151	290	2.53	27.0
18	■	——	BCTMP (Rayonier)[g]			250	0.82	23.4
19	♦	— — —	BCTMP (Rayonier)		13	200	0.77	23.5
20	▲	· · · · · ·	BCTMP (Rayonier)		30	128	0.72	23.7
21	■	——	TMP (West Fraser)[h]			720	1.64	36.7
22	▲	· · · · · ·	TMP (West Fraser)		56	680	1.63	36.6
23	♦	— — —	TMP (West Fraser)		112	580	1.59	36.4
24	●	— · — · —	TMP (West Fraser)		229	390	1.50	35.6
25	□	· · · · · ·	TMP (Papier Masson)[i]		37	215	1.00	31.7
26	◊	— · — · —	TMP (Papier Masson)		73	160	0.87	30.9
27	◯	—— —— ——	TMP (Papier Masson)		110	126	0.82	30.9
NF[a]	★	——	Nylon Fibre				3.05	13.6

[a] Also reported in [15].
[b] A northern bleached softwood Kraft pulp (NBSK) comprised of a mixture of pine and spruce wood fibres [34] obtained from Canfor Pulp (Prince George, BC Canada).
[c] A northern bleached softwood Kraft pulp (NBSK) comprised of a mixture of pine and spruce wood fibres [34] obtained from SCA from their Östand Mill (Sundsvall, Sweden).
[d] Southern beached Kraft Pulp (SBK) comprised of a mixture of southern pines [34] obtained from Resolute Pulp from their Catawba mill (SC USA).
[e] Hardwood bleached Kraft pulp comprised of aspen wood fibre obtained from Domtar Corporation (Montreal, QC Canada).
[f] Hardwood bleached Kraft pulp comprised of eucalyptus wood fibre obtained Fibria Celulose (São Paolo, Brazil).
[g] Bleached chemi-thermo mechanical pulp (BCTMP) comprised of a mixture of spruce and fir obtained from Rayonier Advanced Materials (Temiscaming, QC Canada).
[h] Thermo-mechanical pulp (TMP) comprised of lodgepole pine and white spruce obtained from West Fraser (Quesnel, BC Canada).
[i] Thermo-mechanical pulp (TMP) comprised of a mixture of black and white spruce and balsam fir obtained from Papier Masson mill (Gatineau, QC Canada).
[j] EKA FIX 41. All polymer solution were added at 0.1 % (wt/wt fibre)
[k] EKA PL 1510
[l] EKA PL 1510 + EKA NP 320
[m] Fennobond 3300E
[n] Fennosil ES325

Fibre Quality Analyser (FQA). Also listed is the Canadian Standard Freeness (CSF) value, a simple, industrially relevant drainage test in which a suspension is dewatered under the action of gravity. Detailed modelling of this test and efforts to relate its results to the material properties for a single pulp can be found in [27]; we reconsider this quantity for the entire library in §IV-D.

The content and rationale behind the library are illustrated further in figure 1. Before immersing ourselves in these details, however, we pause to outline some background on the pulping processes and subsequent refinements in order to inform that discussion. As mentioned previously, wood fibres vary in length, width, and wall thickness, with a complicated dependence on tree species and origin, stemming from differences in genetics and growing conditions. Typically, fibres from softwood trees (conifers) are longer, wider, and have greater wall thickness than those from hardwoods (deciduous) [35]. The process of separating the fibres from the wood matrix is referred to as pulping, and two broad methodologies exist for the task. Chemical pulping dissolves the lignin-rich layers that bind the fibres together. The dissolution also removes substantial quantities of lignin and some hemicellulose from the main body of the fibre wall, enhancing the fibre wall's porosity, and exposing cellulose fibrils that attract water molecules to the free hydroxyl groups [36]. Kraft pulping is used exclusively in this work, where fibre liberation occurs by addition of sodium sulfide to a wood chip under alkaline conditions. Thermo-Mechanical pulping (TMP) takes a cruder approach of bashing and cracking the matrix of wood chips by shear, created in the gap between two closely spaced patterned-discs rotating at different rates. This process avoids any significant dissolution of the fibre wall, but also fractures the solid structure, reducing fibre lengths and producing a high content of fines, which are primarily flakes from the middle lammelae. As a result, the water content of the fibre wall is typically lower and the fibres are stiffer than chemically pulped fibres [37]. A common variation of this process is a chemi-mechanical pulp, where the lignin is partly dissolved, using a chemistry different than the Kraft process, before mechanical treatment (BCTMP). Beyond the pulping process, the morphology of fibres are modified further by either chemical or mechanical means to modify dewatering performance. Chemical refinement introduces polymeric additives to control surface chemistry and the degree of flocculation, while the second mechanical refinement is another brute-force approach, aimed at creating fibrillation in the fibres both internally and externally; this mechanical treatment is typically referred to as beating or low-consistency refining (LCR).

Overall, we therefore expect a dependence of fibre microstructure and macroscopic material behaviour on wood type, pulping process and refinement. Consequently, the library includes several softwood and hardwood fibres, pulped both chemically and mechanically, and with different degrees of subsequent chemical and mechanical refinement. In the graphical summary in figure 1, we plot the mean aspect ratio of the fibres (defined as length to half-width, $2L/W$); the ordering of the series is chronological and has no other significance. The library begins with three chemically pulped softwoods. Two chemically pulped hardwoods then appear (aspen and eucalyptus; Series 4-5). Series 5 (eucalyptus) was then mixed with Series 1 (Northern Bleached Softwood Kraft, or NBSK) to produce a series of chemical pulps (6-9) with varying fibre geometry. NBSK was then refined chemically (Series 10-14) with various commonly used additives, or mechanically to varying degrees (Series 15-17). The remaining pulps are all processed mechanically: Series 18-20 are hardwood BCTMP and Series 21-27 are softwood TMP with varying degrees of low-consistency refining energy.

In figure 1, the pulps are grouped into three families (as indicated by colour), which represent chemical pulps with no mechanical refinement (light red), chemical pulps with mechanical refinement (purple), and mechanical pulps (blue); the significance of these groupings will be exposed in §III. The fibre aspect ratios vary from about 50 to 200 across the library. Also plotted is the ratio between an effective radius based on the fibre linear density, R_{eff}, and the mean fibre half-width $W/2$. The density-based effective radius R_{eff} (which is also provided by the FQA) is about one half of $W/2$, which provides a rough measure of the porosity contained within the hollow fibre wall. Lastly, note that within each family in the library there appear to be correlations between the mean fibre length and width, as illustrated by the inset of figure 1.

Table I and figure 1 also include data for a suspension of nylon fibres in glycerin. This inclusion provides a more ideal yardstick against which to compare the pulps. Four of the twenty-seven pulps, as well as the nylon suspension, were used previously in [15]. As indicated in table I, each pulp suspension is given a corresponding symbol used throughout to display the results, and a line style for the fits of the material properties.

B. Two-phase modelling

To describe the pulp suspension as a two-phase medium, we identify the fibre network as a solid phase, and the water both between and within the fibres as a fluid phase. Individually, both phases are incompressible. Following our previous study [15] and as illustrated in Fig. 2a, we explore the behaviour of consolidating pulp suspensions using a relatively simple, uniaxial compression test with a porous piston. In this setup, a uniform, networked suspension at an initial solid volume fraction ϕ_0 is dewatered by driving the permeable piston down at a constant velocity V. The load required to maintain this speed, $\sigma(t)$, is a measured output. If the local solid volume fraction is $\phi(z,t)$, implying

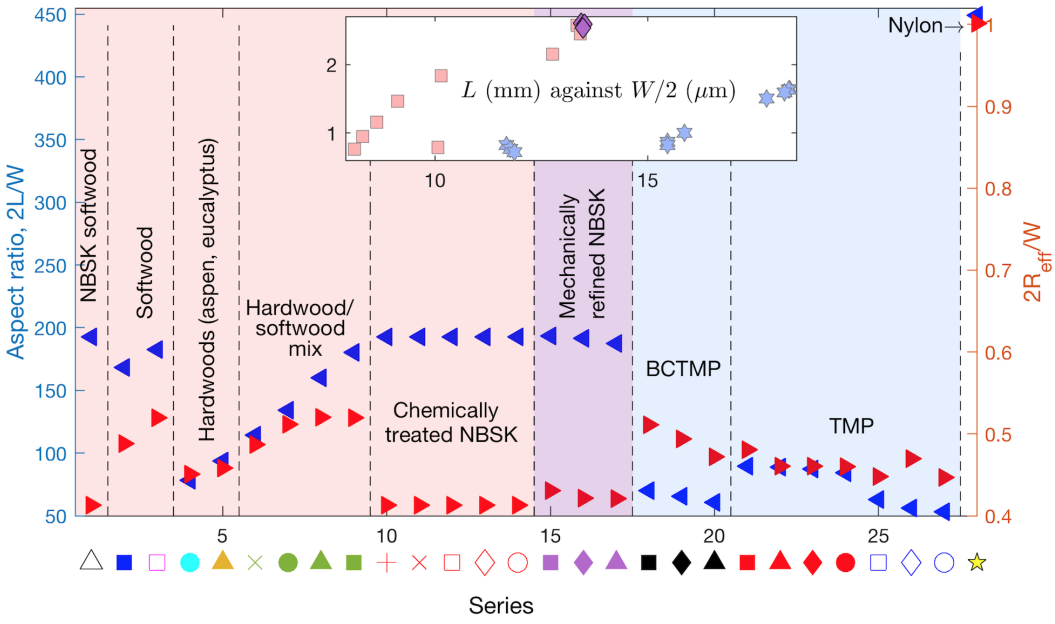

FIG. 1: Pictorial representation of the pulp library, plotting the mean fibre aspect ratio $2L/W$ and the ratio of the linear density-based effective radius R_{eff} to half-width $W/2$, which provides a proxy for the porosity contained within the fibre. The light red, purple and blue colouring identifies three families of pulps discussed in §III. The inset shows a rough correlation between L and $W/2$, with the points coloured by family.

stress-free conditions on the side walls of the container, conservation of mass demands that

$$\frac{\partial \phi}{\partial t} + \frac{\partial}{\partial z}\left(\phi v_s\right) = 0, \tag{1}$$

$$-\frac{\partial \phi}{\partial t} + \frac{\partial}{\partial z}\left[(1-\phi)\, v_l\right] = 0, \tag{2}$$

where v_s and v_l are the solid and liquid (vertical) velocities. Fluid motion through the network is governed by Darcy's law,

$$(1-\phi)(v_s - v_l) = \frac{k(\phi)}{\mu}\frac{\partial p}{\partial z}, \tag{3}$$

given the neglect of gravity and inertia (see [15]). Here p and μ are the pore pressure and viscosity of the fluid, and the permeability $k(\phi)$ is discussed in §II C below.

Following Terzaghi's principle [38], we write bulk conservation of stress in the form,

$$\frac{\partial}{\partial z}\left(p + \mathcal{P}\right) = 0, \tag{4}$$

where $\mathcal{P}$ is the solid network's effective (compressive) stress. As suggested previously [15, 16, 27, 28, 32], we take the latter to be given by the viscoplastic constitutive law,

$$\begin{cases} \mathcal{P} = P_y(\phi) - \eta(\phi)\partial v_s/\partial z & \text{if} \quad \mathcal{P} \geq P_y(\phi) \\ \partial v_s/\partial z = 0 & \text{otherwise} \end{cases}, \tag{5}$$

where $P_y(\phi)$ is the compressive yield stress (discussed further in §II D); $\eta(\phi)$ plays the role of a solid bulk viscosity, which is expected to be $O(\mu)$ if it stems from the motion of the solid through the viscous fluid of the suspension [16]. This Bingham-like constitutive model, similar to laws proposed for single-phase models of fibre suspensions in shear (*e.g.* [39]), incorporates an unyielded state for $\mathcal{P} < P_y(\phi)$ in which collapse is prevented (demanding $\partial v_s/\partial z \equiv \phi^{-1} D\phi/Dt = 0$, where D/Dt is the convective derivative following the solid phase), and a yielded state for $\mathcal{P} > P_y(\phi)$.

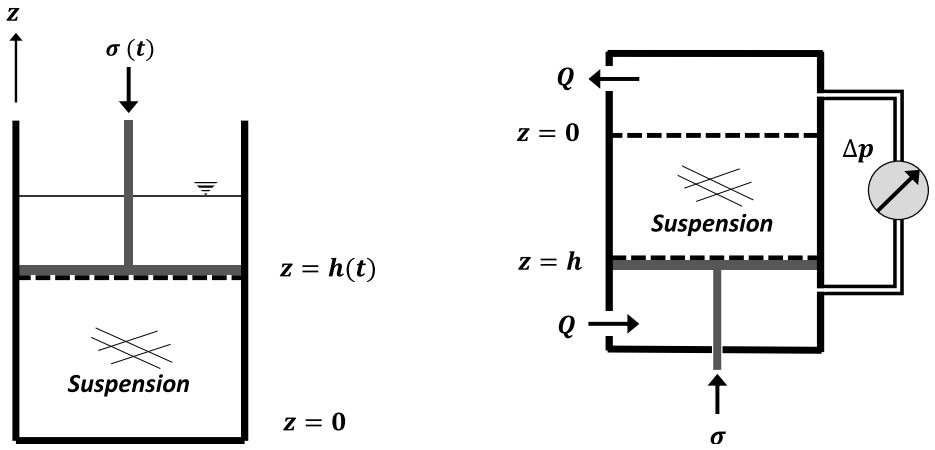

FIG. 2: The geometry of the dewatering experiment is shown in (a). The permeable piston, imposing a load $\sigma(t)$ at $z = h(t)$, compresses the suspension contained in a closed base cup. The permeability apparatus is sketched in (b). The permeable piston, imposing a load σ at $z = h$, holds the compressed suspension in a chamber with a permeable top. Fluid flows with rate Q through the suspension under a pressure drop Δp.

Equations (1)-(5) are solved over $0 < z < h(t)$, subject to the initial and boundary conditions,

$$\phi(z, 0) = \phi_0, \ 0 < z < h_0, \tag{6}$$

$$v_s(0, t) = 0, \quad \text{and} \quad v_s(h, t) = \mathrm{d}h/\mathrm{d}t = -V, \tag{7}$$

where the height of piston is $h(t)$ at time t, and $h(0) = h_0$ initially. The load on the piston is

$$\sigma(t) = P_y(\phi) - \eta(\phi) \left. \frac{\partial v_s}{\partial z} \right|_{z=h(t)}, \tag{8}$$

which may be compared to experimental measurements.

The rapidity of dewatering and the strength of the bulk viscosity are gauged by the two dimensionless groupings,

$$\gamma = \frac{p_* k_*}{\mu h_0 V}, \qquad \epsilon = \frac{k_* \eta_*}{\mu h_0^2}, \tag{9}$$

(*cf.* [15]), where p_*, k_* and η_* denote typical scales for the compressive yield stress, permeability and bulk viscosity, respectively, that will be defined subsequently. Importantly, the parameter γ provides a measure of the role of Darcy drag in resisting compression: if γ is large, the compression becomes quasi-static, the solid fraction becomes uniform in depth, and the load measured on the piston provides a direct measure of the compressive strength of the suspension.

C. Permeability calibration

The permeability apparatus is sketched in figure 2b: the pulp suspension is contained between a permeable surface and piston, located at $z = 0$ and $z = h$, respectively. The hydraulically-driven piston is capable of a maximum compressional load of 1 MPa. With the suspension retained between the surfaces, the height of the piston sets the average volume fraction $\bar{\phi} = \phi_0 h_0/h$. Critically, both the imposed load σ and the height h are corrected for the compliance of the equipment [24]. A flow rate Q of reverse-osmosis water is recirculated through the compressed fibre network from a water reservoir while the pressure drop Δp across the suspension is measured. The water reservoir is held under a vacuum throughout the experiment, maintaining a dissolved oxygen content below 5 ppm and a heat exchanger is used to maintain the temperature at approximately $20°C$. The permeable surfaces are stainless steel discs with repeating arrays of 0.66 mm diameter holes spaced 1.5-2 mm apart, resulting in an open area of approximately 11% (results with other permeable surfaces showed no significant differences). The cross-sectional area of the chamber

is $A = 81.07\ cm^2$.

We extract the permeability as a function of $\bar{\phi}$ from the measurement of Δp according to

$$k(\bar{\phi}) = \frac{Q\mu h}{A\Delta p}, \tag{10}$$

(see [15] for a discussion on the range of validity of this equation). Typical trials use 500-1000 g of pulp suspension with $\phi_0 = 0.02 - 0.03$, and collect measurements at 5 to 10 different values of h. For all experimental calibrations, the pulp suspensions were re-slushed using standard TAPPI protocols (reference number T262) to prepare a desired ϕ_0. Further details of suspension preparation can be found in [24]. At least four trials for each pulp suspension were performed to accommodate experimental variability. Our results for specific pulp varieties are consistent with previous studies (*e.g.* [11–14, 40, 41]).

The results collected are fit to the functional form

$$k(\phi) = \frac{k_*}{\phi} \ln\left(\frac{1}{\phi}\right) e^{-b\phi}, \tag{11}$$

with the characteristic scale k_* and parameter b estimated by linear regression. This form, which conveniently captures the collapse of Jackson & James [10] over their entire range of solid fraction (see §III A), combines the expected permeability law in the limit of a dilute suspension of solid rods [10] with an exponential factor that suppresses $k(\phi)$ at high solid fraction, similar to fits used previously for pulp [14, 15, 41].

D. Compressive yield stress calibration

The compressive yield stress is calibrated using the uniaxial dewatering equipment shown in figure 2a. The cup has a cross-sectional area of 50 cm^2, and 250 – 275 g of pulp suspension with $\phi_0 = 0.02 - 0.03$ was used. The permeable surface of the piston is the same as that used in the permeability cell. The piston is driven by the hydraulic actuator of an MTS 858 tabletop material tester, which has a control unit that performs uniform rate compression tests. The usable stroke of the piston is approximately 60 mm, with its location recorded throughout the experiment. Compressive loads $\sigma(t)$ are limited to maximum values of about 1.2 MPa, and are measured by a load cell at the base of the cup. The piston height and compressive load are corrected for compliance and drag from the piston's seal, respectively (see [24] for further details).

At sufficiently slow rates of compression ($V \equiv \mathrm{d}h/\mathrm{d}t = 1\mu m/s$) the Darcy drag and rate-dependent solid stress are expected to be negligible, implying that the solid remains uniform in depth, with $\bar{\phi}(t) = \phi_0 h_0/h(t)$, such that the load at the piston (equation (8)) is $\sigma \approx P_y(\bar{\phi})$. Measurements are averaged over four separate trials, and following [1, 15], fitted to a functional form

$$P_y(\phi) = \frac{p_*\phi^n}{(1-\phi)^q}, \tag{12}$$

with the characteristic scale p_* and parameters n and q estimated by linear regression. This form combines a power-law behaviour in the numerator like that traditionally adopted for pulp and other materials (*e.g.* [22, 42]), with a term in the denominator that steepens the stress law at higher solid fractions and builds in a divergence as the solid fraction gets large, similar to the Krieger-Dougherty modification of Einstein's viscosity for a suspension of spherical particles [43]. With measurements of k_* and p_* in hand, we confirm that the compressive yield-stress calibrations are performed quasi-statically by computing the dimensionless grouping γ in (9) and verifying that $\gamma \gg 1$. As noted in [15], our measurements of $P_y(\phi)$ are similar to previous studies (*e.g.* [1, 25]).

E. Dewatering tests and bulk viscosity calibration

Having calibrated $k(\phi)$ and $P_y(\phi)$, rapid dewatering tests were conducted in order to investigate to what extent the suspensions exhibit rate-dependent stresses. These experiments differ from the compressive yield stress calibration described above only in the driving rate V of the piston, and the protocol discussed above was also used here. Typically, four different compression rates were chosen for each suspension, with the maximum piston speed V being limited to 10 mm/s. Tests terminated when the load passed 1.2 MPa. For each compression rate, experimental uncertainty was again accommodated by averaging over four duplicate trials. All the experiments used 250 – 275 g of pulp suspension with $\phi_0 = 0.02 - 0.03$.

TABLE II: Fitted material parameters, showing k_* and b in the permeability fit (11), the parameters p_*, n and q for the compressive yield stress fit (12), the optimal value of η_*, and the range of experimental values of the dimensionless piston speed γ (9) used to calibrate η_*.

	Permeability		Compressive Yield Stress			Bulk viscosity	
Series	k_* $[m^2]$	b	p_* [MPa]	n	q	η_* [$MPa\ s$]	γ
1 △	3.60×10^{-13}	18.52	0.67	1.89	2.98	10.0	529 - 0.534
2 ■	2.67×10^{-13}	20.38	0.62	1.87	3.83	28.6	12.0 - 0.297
3 □	5.67×10^{-13}	21.19	0.77	2.04	3.62	11.6	36.8 - 0.920
4 ●	2.76×10^{-13}	14.06	1.31	2.23	2.13	8.71	730 - 0.721
5 ▲	8.12×10^{-14}	19.74	1.05	2.11	3.02	73.6	6.27 - 0.146
6 ×	9.43×10^{-14}	19.42	0.87	2.03	3.19	63.5	5.94 - 0.139
7 ●	1.21×10^{-13}	18.89	0.70	1.95	3.36	32.5	6.26 - 0.162
8 ▲	1.63×10^{-13}	19.11	0.64	1.91	3.54	26.4	7.79 - 0.197
9 ■	2.12×10^{-13}	19.06	0.51	1.81	3.69	21.5	8.00 - 0.205
10 +	1.89×10^{-13}	14.21	0.70	1.99	3.09	7.92	10.0 - 0.254
11 ×	3.72×10^{-13}	13.72	0.84	2.13	2.86	3.53	24.1 - 0.599
12 □	5.28×10^{-13}	14.25	0.69	1.98	3.05	8.84	27.9 - 0.702
13 ◊	2.43×10^{-13}	17.77	0.43	1.72	3.77	20.6	8.33 - 0.199
14 ◯	2.69×10^{-13}	16.37	0.78	2.16	3.12	12.5	16.2 - 0.393
15 ■	1.19×10^{-14}	22.99	0.39	1.82	4.42	661	1.81 - 0.359
16 ♦	8.54×10^{-15}	25.74	0.31	1.70	4.76	5224	5.31 - 0.207
17 ▲	6.02×10^{-15}	25.72	0.24	1.61	5.16	4495	2.83 - 0.282
18 ■	1.62×10^{-14}	22.91	1.62	2.12	2.87	323	1.80 - 0.209
19 ♦	1.21×10^{-14}	24.99	1.34	2.04	3.45	338	2.78 - 0.282
20 ▲	1.65×10^{-14}	26.14	1.30	2.03	3.30	1112	7.41 - 0.719
21 ■	2.41×10^{-14}	21.22	3.93	2.20	1.09	329	6.81 - 0.154
22 ▲	1.28×10^{-14}	15.27	3.89	2.25	1.01	174	3.42 - 0.096
23 ♦	3.56×10^{-14}	21.22	3.16	2.18	1.34	211	8.34 - 0.191
24 ●	1.35×10^{-14}	19.08	2.83	2.20	1.31	284	2.83 - 0.082
25 □	9.71×10^{-15}	18.19	2.68	2.29	2.06	109	9.65 - 0.504
26 ◊	2.36×10^{-15}	16.55	1.40	1.99	2.76	692	1.26 - 0.149
27 ◯	1.47×10^{-15}	23.10	1.66	2.09	2.48	5609	1.82 - 0.166

To determine the bulk viscosity function $\eta(\phi)$, we first note that some success in reproducing the dewatering dynamics of pulp suspensions has be achieved using the functional form,

$$\eta(\phi) = \eta_* \phi^2 \tag{13}$$

[15, 27, 44], where the constant $\eta_* = O(10^7) Pa \cdot s$. We continue with this form here, and estimate the parameter η_* for each pulp from our experimental data as follows. Given the load $\sigma_{Exp}(t; V)$ averaged over each of the four duplicate trials for each compression speed V, we minimize the objective error function $\mathcal{F}$,

$$\mathcal{F}(\eta_*) = \big\langle \mathcal{E}(\eta_*, V) \big\rangle, \qquad \mathcal{E}(\eta_*, V) = \frac{\int \left| \sigma_{Model}(\bar{\phi}; V, \eta_*) - \sigma_{Exp.}(\bar{\phi}; V) \right| d\bar{\phi}}{\int \sigma_{Exp.}(\bar{\phi}; V) d\bar{\phi}}, \tag{14}$$

where time t has been converted into the mean solid fraction via $\bar{\phi} = \phi_0 h_0 / h(t)$, and $\sigma_{Model}(\bar{\phi}; V, \eta_*)$ is the predicted stress from the model. The angular brackets $\langle \cdots \rangle$ represent an average over all the different experimental compression speeds V. Based on the range of η_* that gave values of $\mathcal{F}$ within 5% of the minimum, we report an uncertainty of approximately 20% in our estimates for η_*.

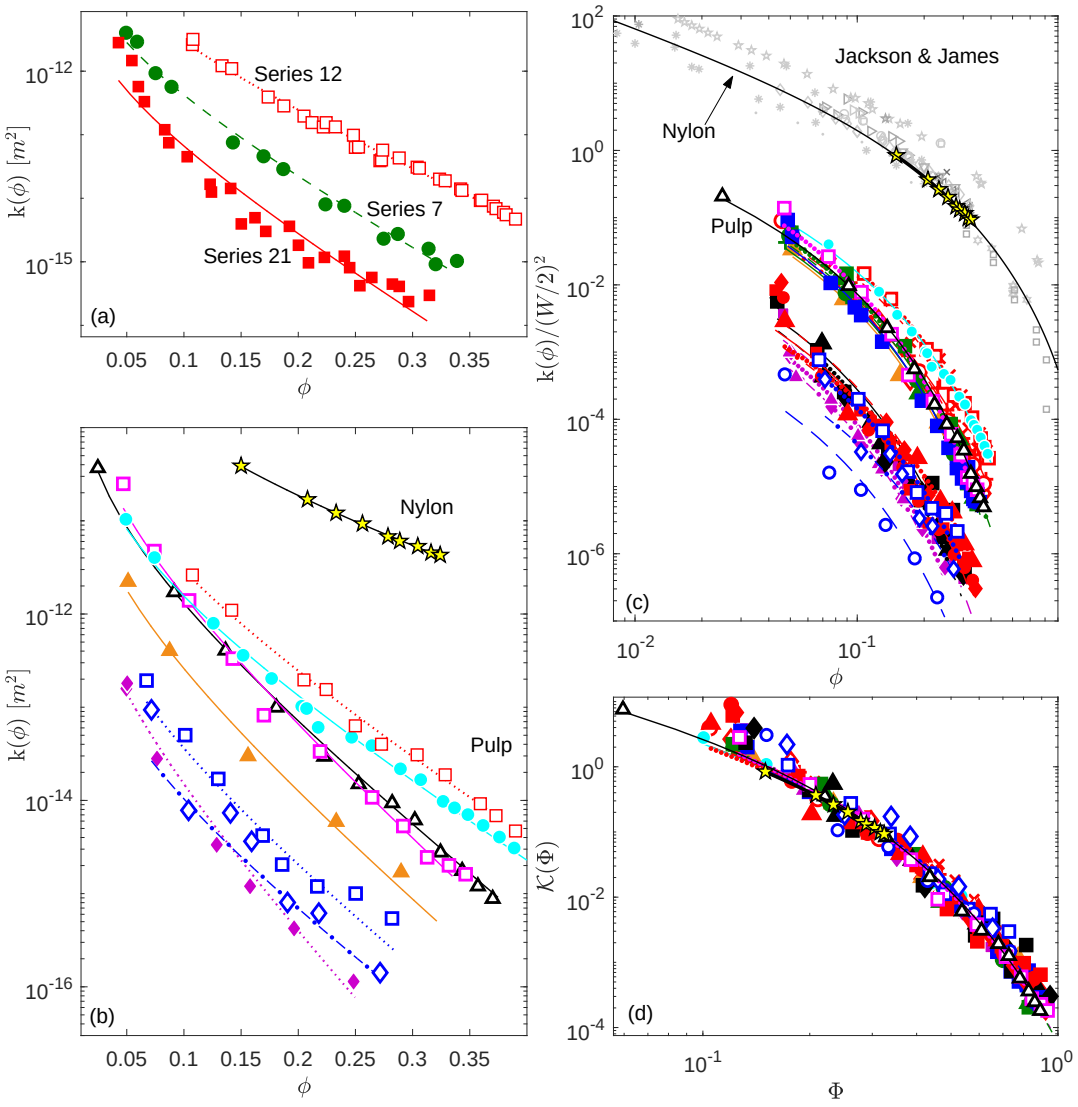

FIG. 3: (a) Permeability results and fit (11) for well-fit, typical and poorly-fit suspensions (Series 12, 7 and 21 respectively). (b) Permeabilities for a representative subset of the library (Series 1 (△), 3 (□)), 4 (●), 5 (▲), 12 (□), 16 (♦), 25 (□), 26 (◇). (c) Scaled permeabilities for all the pulps. The cloud of small gray symbols represent the bulk of the compilation of Jackson & James [10]. (d) Scaled permeabilibity, $\mathcal{K} = k/\alpha^2$, against scaled solid fraction, $\Phi = \beta\phi$, for the entire pulp library; the scaling parameters α and β are plotted in figure 4.

III. RESULTS

A. Permeability, $k(\phi)$

The measured permeabilities of the pulp suspensions are shown in figure 3 and compared with that for nylon; the fitting constants k_* and b of (11) are listed in table II. Figure 3(a) illustrates the variability of the experimental measurements about some mean curve and the quality with which that curve is fit by (11) for Series 12, 7 and 21, which provide examples of relatively good, average and poor fits, respectively. A more representative selection of pulp permeabilities is shown in figure 3(b). For each suspension, the symbols represent sample measurements (we avoid showing all of the data points for clarity) and the lines show (11). These representative results show significant variation across the pulp suspensions, with considerable differences in magnitude and more subtle variations in trend, similar to previous findings. Moreover, the pulp permeabilities are all much less than that for nylon (figure 3(b)).

A key step taken by Jackson & James [10] was to recognise that the greatest variability between the permeability of

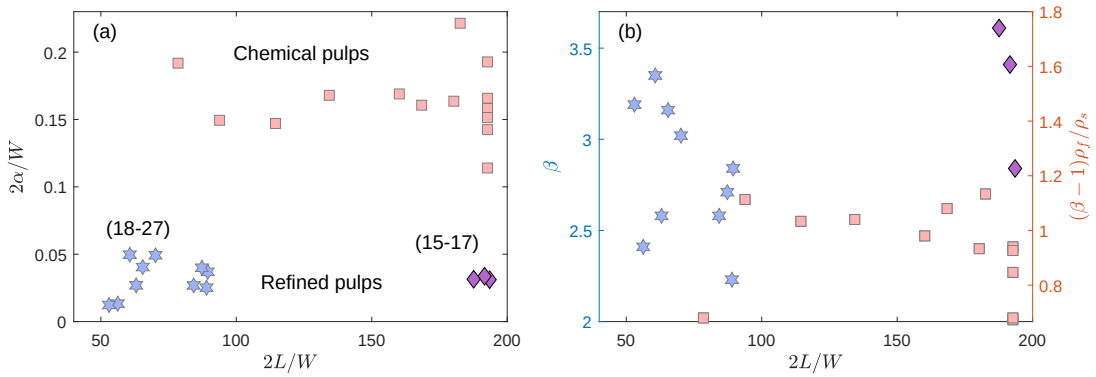

FIG. 4: The scaling parameters (a) α and (b) β of the pulp permeability data used in figure 3(d), as defined in (16). In (b), the solid volume fraction scaling is re-interpreted on the right-hand axis as the water-retention-value-like quantity $(\beta-1)\rho_f/\rho_s$, where ρ_f and ρ_s are the fluid and solid densities (see discussion in §IV A). The scaling parameters are plotted against the mean fibre aspect ratio $2L/W$, and the symbol/colour scheme follows that given in figure 1.

different fibrous porous media was due to a difference in the characteristic length-scale controlling flow (*i.e.* the pore size). For relatively straight and rigid, large aspect ratio, uniformly sized rods, this length-scale is the fibre radius R, and a scaling of $k(\phi)$ by R^2 achieves the Jackson & James collapse. In figure 3(c), we follow the Jackson & James scaling, using the mean pulp half-width $W/2$ measured by the FQA in place of R. This figure also shows the bulk of the data compiled by Jackson & James, which includes nylon fibres, wools, wire crimps, and filter pads. The plot demonstrates how Jackson & James's compilation collapses to within a band whose thickness (on the logarithmic plot) is less than a factor of about ten, whereas the original permeabilities varied by several orders of magnitude. Jackson & James argued that the remaining scatter is due to variations in fibre orientation, cross-sectional shape of the particles, and homogeneity of the porous network.

The permeability of our nylon fibres does indeed fall within the Jackson & James band, confirming how this material conforms to the ideal norm of a fibrous porous medium. Evidently, as demonstrated in figure 3(c), pulp does not conform to this scaling, perhaps because its microstructure falls far short of the restrictions imposed by Jackson & James when compiling their data: pulp fibres are polydisperse, non-circular, and curved or bent. Worse still, the hollow fibres may partially or fully collapse as the suspension is consolidated [22, 45], leading to either tube-like particles or flattened ribbon structures. Irrespective of this, two rough groupings of the series do seem to be evident in figure 3(c): the chemically pulped hardwoods and softwoods become broadly aligned with one another and are noticeably more permeable than the mechanically pulped and refined chemically pulped suspensions. These groupings are those that were previously identified in figure 1, where the group of chemical pulps is coloured red, and the others are highlighted in blue and purple.

Despite the failure to align the permeabilities of our pulp suspensions with either themselves or other, more ideal fibrous porous media, a two-parameter rescaling of the data can achieve a surprisingly compact collapse. More specifically, our fit of the nylon data is $k = R^2\mathcal{K}(\Phi)$, where

$$\mathcal{K}(\Phi) = \frac{0.147}{\Phi}\ln\left(\frac{1}{\Phi}\right)e^{-5.4\Phi}, \tag{15}$$

and $\Phi \equiv \phi$, which pierces through the centre of the Jackson & James band, even when plotted for values of Φ outside of those used to calibrate the fit (figure 3(c)). Given this functional form, we scale the solid volume fraction and permeability of the pulp data $k(\phi)$ by the factors α and β so that

$$\mathcal{K} = \frac{k}{\alpha^2} \quad \text{and} \quad \Phi = \beta\phi, \tag{16}$$

and then perform a least squares calculation to minimize the difference between $\alpha^{-2}k(\beta\phi)$ and $\mathcal{K}(\Phi)$. The collapse of the data that results is shown in figure 3(d). The numerical values of the scaling parameters α and β are plotted in figure 4. The two families of suspensions are clearly visible in the scaling parameter data, with the chemically pulped softwood and hardwood fibres having values of $2\alpha/W$ over the range $0.15-0.22$, whereas for the mechanically pulped suspensions and refined chemically pulped fibres, $2\alpha/W$ is between 0.02 and 0.05.

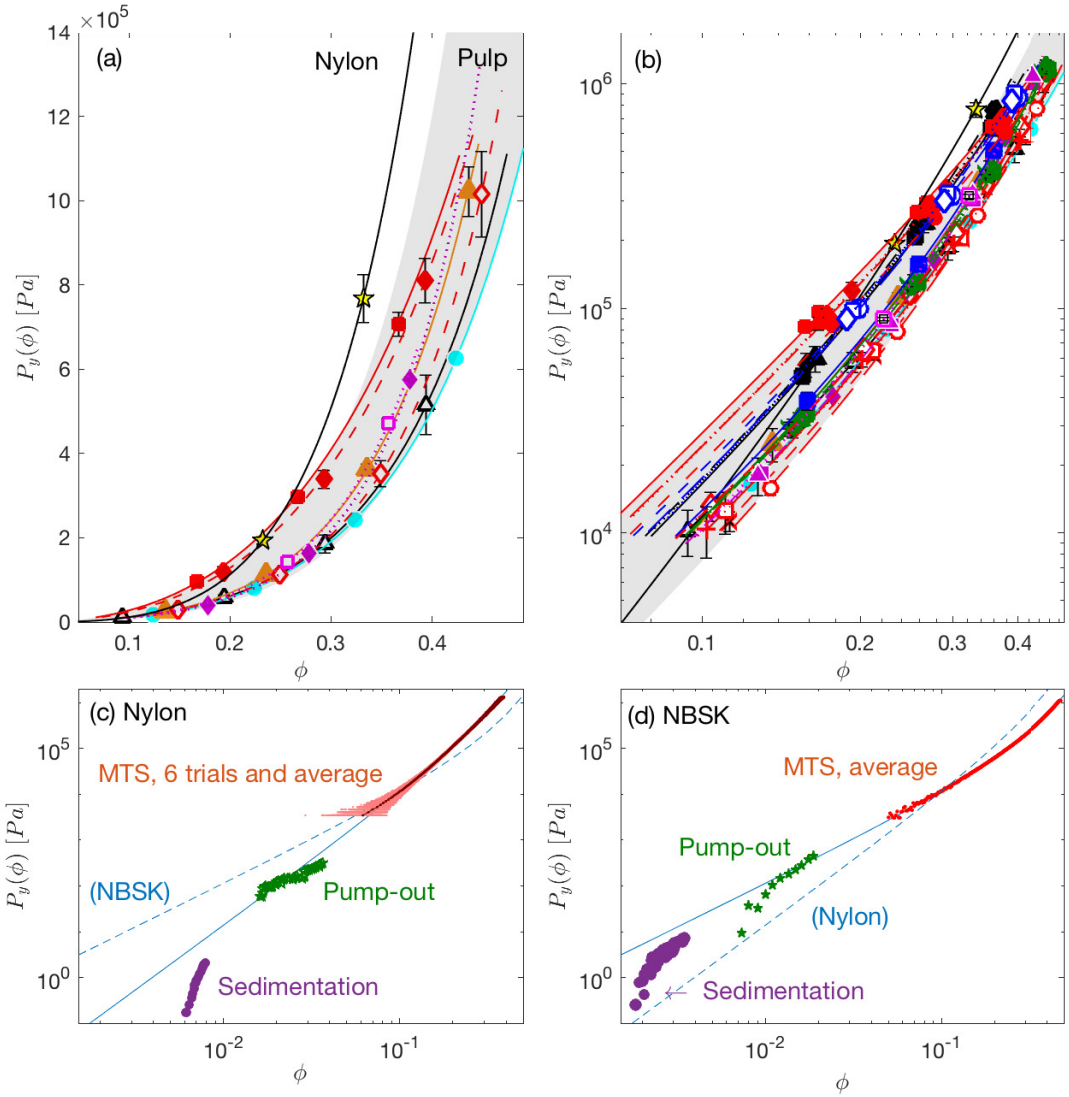

FIG. 5: (a) A representative selection of results for compressive yield stress (Series 1 (△), 3 (□), 4 (●), 5 (▲), 13 (◊), 16 (♦), 21 (■), 23 (♦), and nylon fibers (★)). (b) A plot of $P_y(\phi)$ for the full pulp library. The shaded region spans the range of measurements for pulp according to the fits, and the error bars represent two standard deviations over the repeats of each test. Panels (c) and (d) show P_y data for nylon and NBSK (series 1), respectively, extended to lower concentrations. The fit for NBSK is shown as the dashed line in the nylon plot, and *vice versa*. The "pump-out" data measure the compressive yield stress by withdrawing water from below a suspension held in a vessel with a permeable bottom [27]; the "sedimentation" data come from measuring the final heights h_f from gravitational collapse (plotting $\bar{\phi} \approx \phi_0 h_0/h_f$ against $\phi_0 h_0(\rho_s - \rho_f)g$). In (c), data from six tests with the MTS are showm (lighter red dots), together the average over these tests (darker red dots); in (d) only the average MTS measurements are shown.

B. Compressive Yield Stress, $P_y(\phi)$

In figure 5 we show compressive yield stresses for a representative selection of pulp suspensions and the full library. Again, the symbols display select data points and the line is (12), which admirably fits the data for all 27 pulps. Unlike the permeability, there is relatively little spread in $P_y(\phi)$ across the library, with all the series falling within a factor of about four of one another at any given solid fraction. The logarithmic plot of the data highlights how the dependence on solid fraction extends beyond a simple power law, and supports the functional form of (12). The fitting parameters are tabulated in table II and plotted in figure 6. These display only mild variations across the library. In particular there is little signature of any significant dependence on fibre aspect ratio.

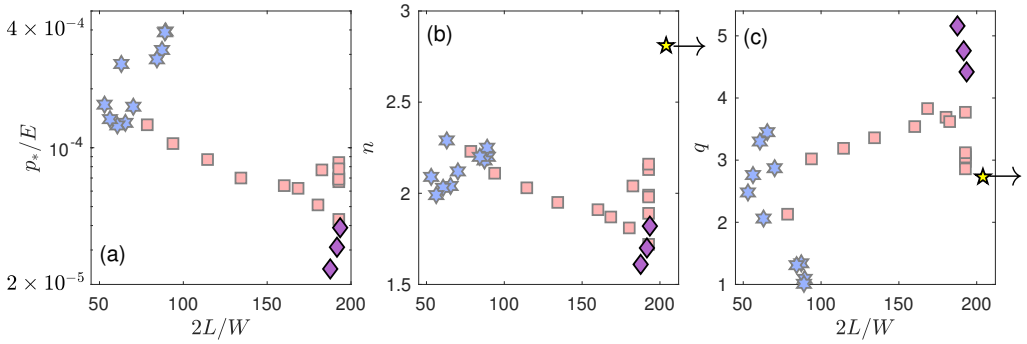

FIG. 6: Characteristic scale and the parameters of the fit for the compressive yield stress in (12), with p_* scaled by the Youngs modulus E (assumed to be 10^{10}Pa for cellulose; for nylon $2L/W \approx 450$ and $p_*/E \approx 0.0057$ if $E = 10^9$Pa)). All the panels plot the fitting constants against the mean fibre aspect ratio $2L/W$, and the symbol/colour scheme follows that given in figure 1.

Qualitatively, the variations in the prefactor p_* follow broad expectations based on microstructural properties: the unrefined chemical pulps are all similar, with the shorter hardwoods being slightly more rigid, and chemical additives have minimal impact (the red squares in figure 6). Mechanically refining the chemical pulps reduces fibre stiffness (and therefore p_*; purple sequence), whereas mechanically pulped fibres are mostly stronger (blue stars).

Figure 5 also shows that the magnitudes of the compressive yield stresses of the pulp suspensions are broadly similar to that of nylon. In detail, however, there is a definite suggestion that the nylon stress rises noticeably faster with ϕ. Indeed, interpreting n as the index of a low-solid-fraction power-law behaviour, we see that the pulps are all consistent with the dependence $P_y \sim \phi^2$, where the nylon is closer to $P_y \sim \phi^3$ (see figure 6(b)). As we discuss later, this distinction may bear on the interpretation of the microstructural origin of this stress. Consequently, to ensure that this conclusion is not an artefact of the fitting procedure over a narrow window of solid fractions, and because our fits of n are slightly lower than previous results for a pulp similar to Series 1 and 3 [1], we have compared the results with some other tests conducted at much lower concentrations. These tests consist either of pumping water out of a suspension held in a container with a permeable base, or monitoring the sedimentation under gravity of the solid from an initial concentration below the gel point. Such tests formed the basis of the low-ϕ calibrations of $P_y(\phi)$ conducted in [27]; here we extend these to nylon and carry over our previous results for pulp series 1. The measurements of $P_y(\phi)$ for these materials, now extended down to much smaller volume fractions, are shown in figure 5(c,d) and are consistent with the fits of the MTS data, modulo a sudden drop-off near the gel point. Importantly, one gains further confidence in the conclusion that $P_y \sim \phi^n$ with $n \approx 2$ for pulp and $n \approx 3$ for nylon at low concentrations. The somewhat higher power-law exponents reported in previous literature (*e.g.* [22, 26, 42]) may have their origin in the use of strongly anisotropic fibre mats, or the use of a single power-law over the entire range of solid fraction which becomes artificially biased if the stress law steepens at higher compactions.

C. Dewatering and bulk viscosity, $\eta(\phi)$

We choose the same three representative series (12, 7, 21) as when presenting the permeability results to illustrate the dewatering behaviour found across the library; again, these series represent relatively good, typical and bad fits to the model (that is, small, typical, and high values of the objective function $\mathcal{F}$ in (14), respectively. Results for these series are shown in figure 7, which plots the instantaneous load $\sigma(t)$ against mean solid fraction $\bar{\phi}(t) = \phi_0 h_0/h(t)$. The figure illustrates the increasing difficulty of dewatering the pulp suspension at higher rates of compaction V (lower values of γ), a feature that is qualitatively similar for the three series. In more detail, at fixed compression rate, series 7 (panel b) is rather harder to dewater than either of the other series (panels a and c), which are themselves somewhat similar. This difference is partly expected, because of the relatively low permeability of series 7 relative to that of series 12 (see table II), although this explanation ignores any potentially differing contributions from the bulk viscosity, as we quantify (and also dismiss) below.

The comparison of series 12 and 21 (panels a and c) is more curious, because their loads are similar but series 21 has a lower permeability even than series 7. In fact, series 21 highlights an experimental challenge that we found for a subset of the mechanically pulped suspensions (Series 21 - 24): these suspensions had a higher content of 'fines', being the fraction of measured fibre lengths less than 0.5 mm, than the other pulp suspensions. The high fines content means that retention of the solid phase underneath the permeable piston is a challenge at elevated compression rates. This

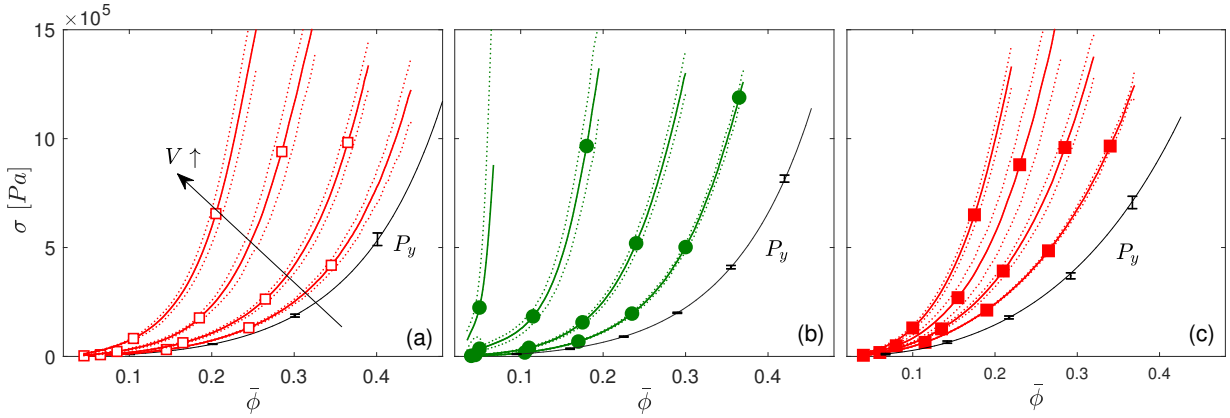

FIG. 7: Compressive load $\sigma(t)$ against average solid fraction $\bar{\phi}(t) \equiv \phi_0 h_0/h(t)$ for Series (a) 12, (b) 7 and (c) 21. Four dewatering experiments are shown as the coloured lines, corresponding to $V = 0.25$, 1.5, 5, and $10\,mm/s$ respectively, with increasing dewatering rates (decreasing values of γ) indicated by the black arrow. The compressive yield stress is shown by the black line. The error bars and dotted lines represent two standard deviations over the multiple repeats of each trial.

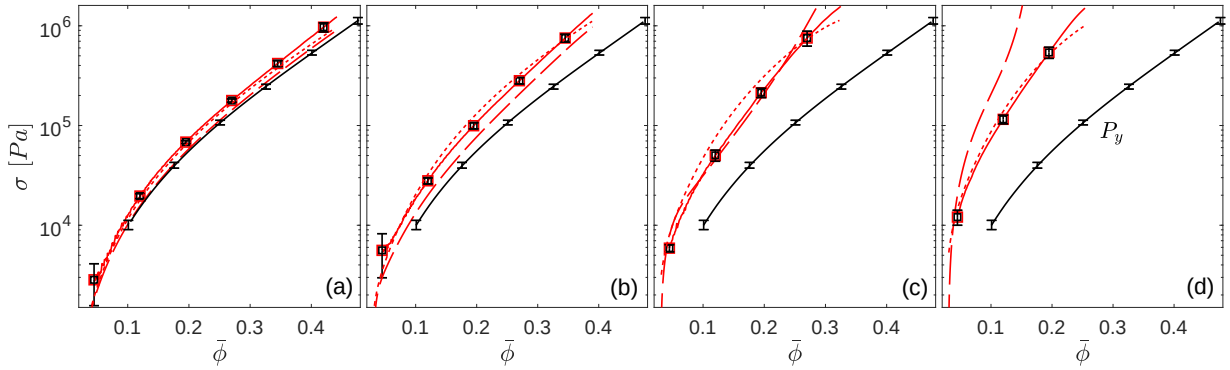

FIG. 8: Series 12 model representation for dewatering rates of (a) 0.25, (b) 1.5, (c) 5, and (d) $10\,mm/s$ ($\gamma = 27.9$, 4.5, 1.4, and 0.70). In each panel, the experimental data are shown by the red solid line, the model result with a fitted bulk viscosity by the red short dashed line, and the zero-bulk-viscosity model by the red long dashed line. The black line shows the compressive yield stress.

was evident visually after the experiment by the cloudiness of the water above the piston. The ineffective retention of the solid phase implies that the measured compression load was probably artificially low during dewatering, a problem commonly encountered in industry when dealing with mechanically pulped suspensions. For the other mechanical pulps (Series 25-27), these retention issues were less severe.

The successful match for Series 12 between the experiments and the theoretical model (with optimally tuned bulk viscosity parameter) is illustrated in figure 8. Although at the lower rates of compression the model performs well with or without a bulk viscosity, it can only be matched with the experiments at the highest compression rate when the bulk viscosity is included. This conclusion mirrors the findings of Hewitt et al. [15], which they reinforced by comparing observations of the successive displacements of tracers in the solid network with the solid velocity predicted by the model. Crucially, no such conclusion was reached for dewatering tests on the nylon suspension, for which the model without any bulk viscosity sufficed to represent experiments. In other words, for more idealized fibres like nylon, there is little sign of a rate-dependent solid stress, in contrast to pulp.

A more typical example illustrating the match between the model and experiment is provided by series 7, which is shown in figure 9. In this case, the zero-bulk-viscosity model solutions begin to struggle even at lower compression rates. Moreover, although the fitted-bulk-viscosity solutions still represent the experimental results, discrepancies are more noticeable for some of the tests. Despite this, the fitted-bulk-viscosity model evidently remains effective in matching the dewatering experiments.

The overall performance of the model with and without bulk viscosity is quantified in figure 10, which displays the net discrepancy $\mathcal{E}$ defined in (14) for all the tests over the entire library. In this figure, results for the majority of

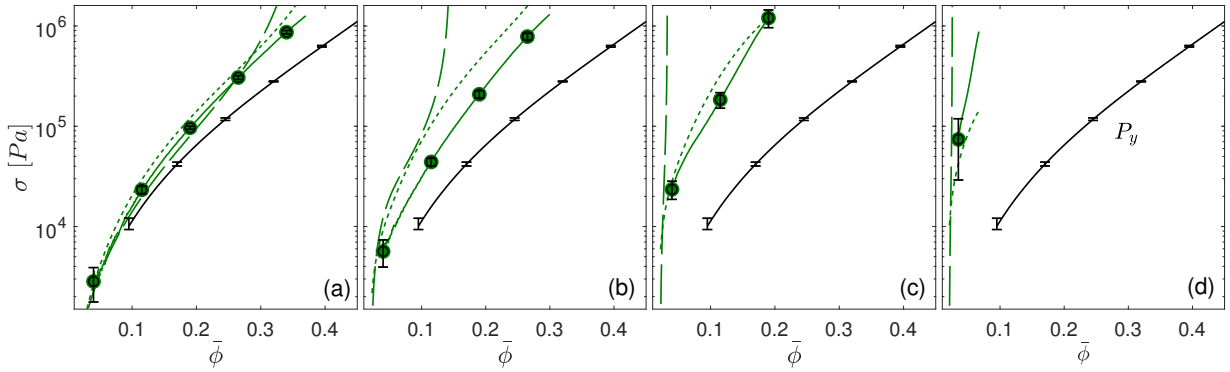

FIG. 9: Series 7 model representation presented for compression rates of (a) 0.25, (b) 1.5, (c) 5 and (d) $10\,mm/s$ ($\gamma = 6.3$, 1.1, 0.32, and 0.16) In each panel, the experimental data are shown by the green solid line, the model result with a fitted bulk viscosity by the green short dashed line, and the zero bulk viscosity model by the green long dashed line. The black line shows the compressive yield stress.

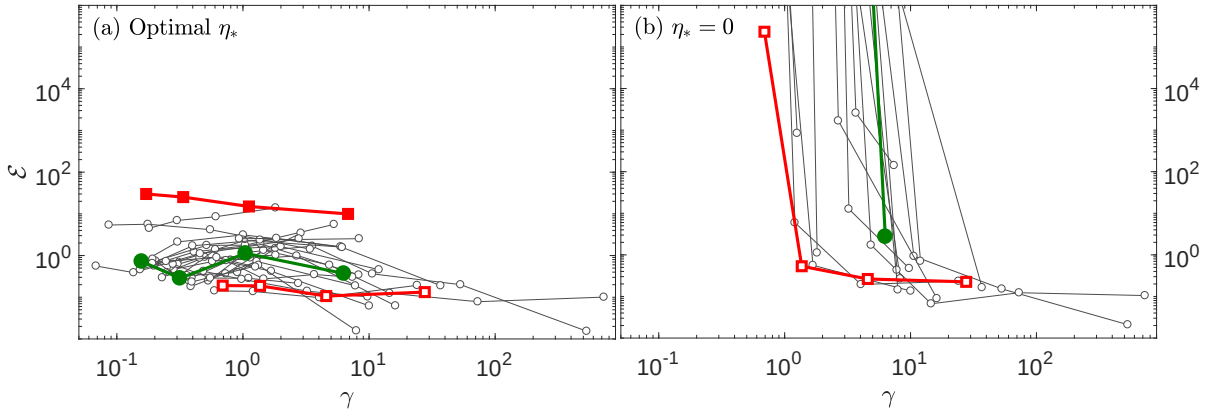

FIG. 10: The error function $\mathcal{E}$ defined in (14) which shows the discrepancy between the experiment and model with (panel (a)) and without (panel (b)) a bulk viscosity, as a function of (dimensionless) dewatering rate $\gamma = p_* k_* / \mu h_0 V$. Series 12 (□), 7 (●), and 21 (■) are highlighted. Points in (b) for which the model cannot be solved due to divergent piston loading (including the entire Series 21) are plotted beyond the axis limits.

the series are plotted in fainter gray, but the three representatives series (12, 7 and 21) are distinguished to reinforce the relatively good, typical and poor performance of the model for these examples. Figure 10(a) shows the values of $\mathcal{E}$ using the optimal value of η_*, whereas figure 10(b) shows $\mathcal{E}$ for $\eta_* = 0$ (no rate dependence). In the latter case, for several series at the fast compression rates (small γ), $\mathcal{E}$ diverges because the model predicts unbounded piston loads $\sigma(t)$ when a highly packed boundary layer forms against the piston, shutting down dewatering (see [15] for a full description of this behaviour). The inclusion of a bulk viscosity therefore not only improves the representation of the experiment by the model, but in many cases allows a model prediction to be made at all.

The optimal values of bulk viscosity parameter η_* for the pulp library are plotted in figure 11. The mechanical and refined pulps have higher bulk viscosities than the unrefined chemical pulps, which are similar for both the soft and hardwoods, and with chemical additives. Otherwise the plot reveals little obvious trend across the library.

A more interesting plot is shown in figure 12, which plots characteristic measures of the permeability, compressive yield stress and bulk viscosity. In particular, although there is no obvious relation between k_* and p_* (panel a), there is a clear correlation between k_* and the bulk viscosity parameter η_* (panel b). In particular, one observes the inverse relation

$$\eta_*[Pa \cdot s] = \frac{5 \times 10^{-6}}{k_*[m^2]}, \tag{17}$$

which was reported with preliminary data by Paterson et al. [27]. Note that the issues with retention noted above lead us to highlight the results for η_* for Series 21-24 in green in both figures 11 and 12, and treat them with some

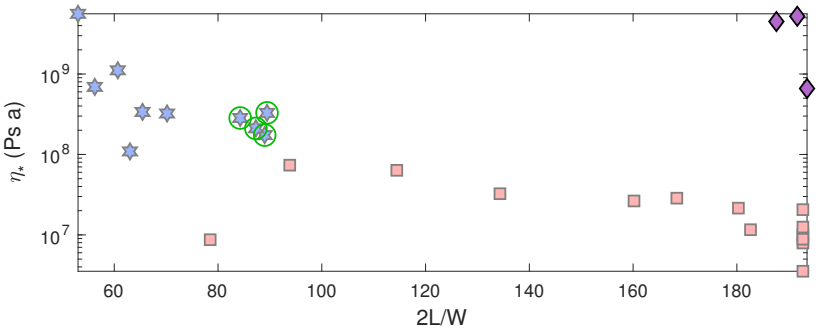

FIG. 11: The optimal bulk viscosity parameter for the pulp library. The points circled in green indicate the series with possible dewatering issues related to the retention of fines, as discussed in the main text.

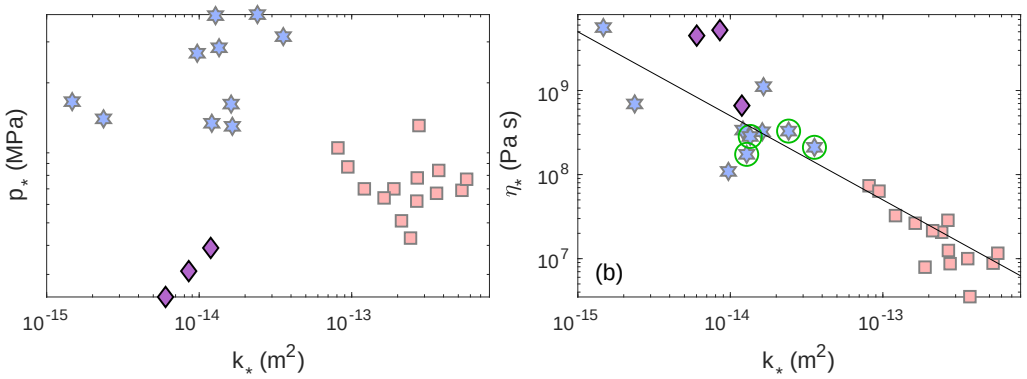

FIG. 12: Correlations between the characteristic scales of the permeability, compressive yield stress and bulk viscosity, plotting (a) p_* and (b) η_* against k_*. The points in (b) circled in green indicate the series with possible dewatering issues related to the retention of fines, and the line shows (17). The colour convention is as shown in figure 1.

caution, although their positions in these plots do not appear to be unusual.

For dewatering tests in general, the bulk viscosity is characterised by the dimensionless parameter $\epsilon = k_*\eta_*/\mu h_0^2$, introduced in (9). The relation in (17) implies that $\epsilon \propto (\mu h_0^2)^{-1}$, which depends only on the fluid viscosity and the initial height of packing. In the various experiments of this study, μ was constant and h_0 varied only marginally, so that $\epsilon \sim O(10^{-1} - 10^0)$. In retrospect, we see that this consistent value of ϵ assisted our calibration of $P_y(\phi)$, which exploits a large $\gamma \gg \epsilon$ limit (see [15]), and ensured that the dynamic dewatering tests operated in the regime where the bulk viscosity was important (*i.e.* mostly to the left of the flat net discrepancy on the right of figure 10(b)). The small range of ϵ also rationalizes why the dewatering behaviour of Series 12 and 7 can be understood primarily in terms of their characteristic permeabilities.

IV. DISCUSSION

A. Permeability

Pulp fibres are hollow, complicated structures with space within the walls that traps water. It is therefore plausible that certain regions of the pore space do not participate in the bulk flow through the network, but form relatively stagnant reservoirs. This viewpoint, which has been advanced a number of times in previous literature (*e.g.* [12, 26, 46, 47]), implies that a fraction of the solvent volume is inaccessible and better viewed as part of the solid, at least until the very highest consolidations. In turn, this suggests that the effective permeability should be equivalent to that of a network with a higher solid volume fraction and a smaller pore scale. It is therefore tempting to interpret the two scaling factors α and β used to collapse our permeability data as those that are required to recover the effective solid fraction and pore size from those based on the dry mass of solid and fibre radius. With this interpretation, $2\alpha/W$ is related to fibre geometry; the relatively low numbers found for this ratio in figure 4(a) suggest that typical

pore scales are rather smaller than the fibre dimensions at the solid fractions of our calibrations. Moreover, the lower permeabilities of Series 15-17 and 18-27 can be attributed to a lower characteristic pore scale prompted by mechanical pulping or refining. It is interesting that $2\alpha/W$ appears to segregate the series into two distinct groups, suggesting both that different chemical treatments have minimal impact on the characteristic pore scale, and that any form of mechanical treatment or refinement results in the emergence of a distinct, lower characteristic pore scale.

Similarly, $\beta\phi$ measures the volume fraction occupied by inaccessible water and must therefore be related to the geometrical factor $2R_{\text{eff}}/W$ plotted in figure 1, which indicates the discrepancy between fibre size and solid content at the microscale. In particular, if water were completely locked inside the fibre, then $\beta \sim (2R_{\text{eff}}/W)^{-2}$. This overestimates the scaling parameter by a factor of order unity, in line with the idea that only some of the water within the fibre is accessible.

The scaling factor β can alternatively be interpreted as the ratio of inaccessible water to dry mass of solid, via $(\beta-1)\rho_l/\rho_s$ (the right-hand axis in figure 4(b)). Two tests are conventionally conducted to quantify more directly the amount of water trapped in the fibre wall. The first, which measures what is termed the "water retention value", is a centrifuge experiment in which a sample suspension is dewatered at a centrifugal force of $(3000 \pm 50)g$ for $15min \pm 30s$ (TAPPI standard reference UM 256). The centrifugal force is assumed sufficient to remove the accessible water, and the trapped water is then determined by drying the sample. A second test calculates the "fibre saturation point" by adding a polymer solution of known concentration to a moist pulp suspension. The polymer has a molecular diameter exceeding the largest pore in the fibre walls, and so only the accessible water dilutes the polymer solution, the total volume of which can be determined from the change in polymer concentration [48]. Although both tests have their limitations [21, 47], there is evidence to suggest that they furnish similar estimates of the amount of trapped water [49]. Those estimates indicate that the amount of trapped water ranges from 0.8 to 2.4g per 1g of solid for typical pulps, which is consistent with the estimates of $(\beta - 1)\rho_l/\rho_s$ in figure 4b.

B. Compressive yield stress

Van Wyck's scaling argument for textile fibres supposes that the solid stress stems from the elastic bending forces resisting the collapse of the network [19]. We briefly review this argument here, following the more recent discussion of Toll [20], then revise it in view of our experimental results. For slender, relatively dilute fibres of length L and typical cross-section width W, the expected number density of contacts scales as

$$n_c \sim \frac{\phi^2}{W^3}, \tag{18}$$

(see also [50, 51]). If each contact point sustains a force f, the bulk stress supported by the micro-structure is

$$P_y(\phi) \sim n_c \Delta f, \tag{19}$$

where Δ represents the typical length-scale of microscopic deformation.

For a contact force stemming from the elastic bending of cylindrical, randomly orientated, relatively dilute fibres, the length-scale for deformation is the typical distance between each contact, $\Delta \sim W/\phi$, and

$$f \sim \frac{EW^4}{(W/\phi)^2}, \tag{20}$$

where E is Young's modulus of the fibre wall [19, 20]. Hence,

$$P_y(\phi) \sim E\phi^3, \tag{21}$$

which is independent of fibre geometry and has been shown to capture the solid-fraction dependence of the solid stress for suspensions of wool [19].

At lower solid fractions, our compressive yield stress data also takes the power-law form $P_y \to p_*\phi^n$. Moreover, for nylon suspensions the exponent $n \approx 3$, suggestive of elastic bending forces providing the restoring forces underscoring the solid stress. The pulp suspensions, however, show a weaker dependence on solid fraction, with $n \approx 2$. Given (18) and (19), a ϕ^2-dependence of $P_y(\phi)$ is suggestive of a contact force f and deformation length-scale Δ that are independent of solid fraction. For example, if elastic deformation takes place over the scale of the fibre radius, such as might arise by a local collapse or buckling of the wall due to the hollow nature of a fibre (*cf.* [22, 45]), then $\Delta \sim W$

and $f \sim EW^2$, giving

$$P_y(\phi) \sim E\phi^2, \tag{22}$$

which aligns with our results in figure 6, both in terms of the power n and the fibre-geometry-independent pre-facter p_*. Thus, pulp fibre structure might underlie the weakening of the $\phi-$dependence of $P_y(\phi)$.

Despite this, the limited recovery of the network on unloading [22–26] argues against an elastic origin to the solid stress. Moreover, our fitted values of the prefactor p_* of the power-law, which should match up with E, are too small by factors of $O(10^{-4} - 10^{-3})$ in comparison to typical values of the Young's modulus for nylon and cellulose of $E = O(10^9)$ and $(10^{10})\, Pa$, respectively; see figure 6. One might argue instead (*cf.* [52]) that frictional rearrangements under elastic normal forces dominate the compressive yield stress, leading to

$$P_y(\phi) \sim \nu E\phi^3 \quad \text{or} \quad \nu E\phi^2, \tag{23}$$

where ν is an effective friction coefficient at the contact points, which might be sufficiently low due to the presence of interstitial fluid to rationalize the relatively small values of p_*/E. Alternatively, for pulp, plastic deformation of the fibre wall at a yield stress of σ_Y might be implied, so that $f \sim \sigma_Y W^2$ and therefore $P_y(\phi) \sim \sigma_Y \phi^2$, as long as σ_Y varies little between pulps. Either way, the relative insensitivity of the compressive yield stress across the entire pulp library, with its various constituents possessing a range of fibre geometries and statistics, points to an underlying microstructural mechanics that must have a universal flavour and transparent origin.

C. Bulk viscosity

Buscall & White [16] argued that the viscous flow of the solvent around a collapsing solid network should translate to a bulk solid viscosity, much as the averaging procedure of two-phase theory generically predicts solid shear viscosities [33]. However, they also argued that such solid viscosities should be insignificant since they will be of the order of the solvent viscosity $\mu = 10^{-3} Pa\ s$, in contrast to our calibration in figure 11. Detailed single-phase constitutive theories for slender fibres [39, 53, 54] also predict shear viscosities of this kind, as well as suggesting a dependence on the fibre aspect ratio that can significantly promote the size.

To provide a model scaling law for the bulk viscosity along the lines of §IV B, we first consider slender cylindrical fibres sliding past one another, separated by a gap of order W. Because entire fibres are in motion, the length scale of deformation is $\Delta \sim L$. The relative velocity between the fibres is $U \sim L\, \partial v_s/\partial z$, and so the viscous shear stress is of order $\mu U/W$, acting over an area of order W^2 when the fibres are inclined to one another. The viscous contact force is therefore $f_v \sim \mu U W$, implying an additional rate-dependent solid stress of

$$\mathcal{P} - P_y(\phi) \sim n_c \Delta f_v \sim \mu \left(\frac{L}{W}\right)^2 \phi^2 \frac{\partial v_s}{\partial z}, \tag{24}$$

which reproduces the scaling of the short-range stress proposed in [54], as well as the ϕ^2 dependence adopted for $\eta(\phi)$ in our two-phase model in (13). However, equation (24) suggests a bulk viscosity scaling of $O(10^{-1} - 10^{1})\, Pa \cdot s$ for aspect ratios $2L/W$ over a range of $50 - 200$, which is much smaller than the calibrated values of η_*. The relatively strong dependence on aspect ratio is also inconsistent with the pulp library (figure 11), and there is no clear connection to the permeability scale k_*.

We therefore turn to a less specific idealization of the collapsing network, using this last point to suggest that the conduits conveying the fluid should have a typical cross-sectional area of k_*. Over the deformation length Δ, solid velocity differences of order $U = \Delta\, \partial v_s/\partial z$ drive fluid down these conduits. Mass balance then demands that the fluid velocity associated with the collapse of the network is $O(\Delta^2 U/k_*)$, and so the associated viscous stress is $\mu(\Delta^2 U/k_*)/\sqrt{k_*}$, acting over the area of the conduit wall $\Delta\sqrt{k_*}$. Thus, $f \sim \mu\Delta^3 U/k_*$, and so

$$\mathcal{P} - P_y(\phi) \sim \mu \frac{\Delta^5}{k_* W^3} \phi^2 \frac{\partial v_s}{\partial z}, \tag{25}$$

which successfully recovers the observed relation between $\eta_* \equiv \mu\Delta^5/(k_* W^3)$ and the permeability scale. However, the choice of the deformation length Δ is not obvious. Taking $\Delta \sim W$ for our pulp library yields $\eta_* \sim \mu W^2/k_* \sim O(10^{-11}) m^2 Pa\ sec$, which is rather smaller than the magnitude that we found in (17). On the other hand, taking $\Delta \sim L$ gives an estimate that is too large, suggesting that the deformation distance lies at some unknown scale between the typical fibre length and width, and indicating that questions still remain about the physical origin of the observed bulk viscosity.

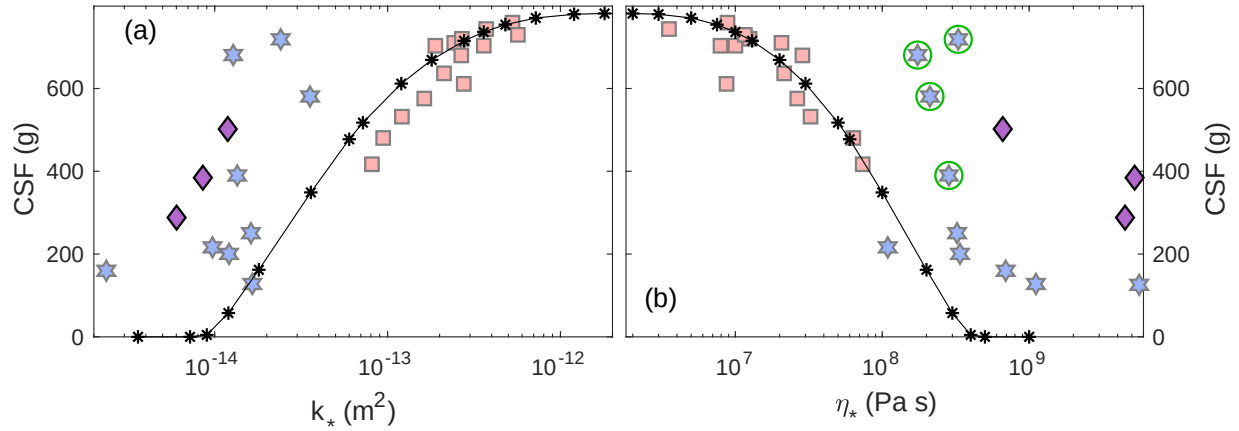

FIG. 13: Canadian Standard Freeness against (a) k_* and (b) η_* for the library results; the solid lines show the theoretical results from [27] (assuming (17)). The points circled in green in (b) again indicate the series with possible dewatering issues related to the retention of fines, which might affect the estimate of η_*.

D. Freeness

Finally, we return to a further measurement made at the outset for the pulp library, the Canadian Standard Freeness (CSF) value (see §II and table I), which is plotted against both k_* and η_* in figure 13. The Freeness test is a simple, table-top-scale gravity-driven drainage test for pulp in which a sample drains through a specially designed funnel. Despite the test's simplicity, the relationship between CSF and any of the material parameters is not immediately transparent. However, Paterson *et al.* [27] previously noted that the CSF value was correlated with η_* for a limited selection of pulps, and confirmed this observation with some detailed modelling of the Freeness test, assuming the bulk-viscosity relation (17). Figure 13 also plots the theoretical prediction from [27], and shows that this correlation (to either η_* or k_*, given their inverse relationship (17)) holds across all the unrefined chemical pulps (red squares). However, the plot again exposes differences between the different 'families' of pulp: evidently the mechanical pulps (blue stars) and mechanically refined pulps (purple diamonds) follow different trends.

The correlation for the unrefined chemical pulps is interesting because it suggests that one can estimate the permeability and bulk viscosity scales simply from the Freeness value. Moreover, given the narrow spread of $P_y(\phi)$ for this particular type of pulp, one could further adopt a nominal choice for this quantity, and thus estimate all the material properties from a single experimental measurement. The story is evidently more complicated with mechanical pulping or refinement, for which pulps with different permeability can still give rise to comparable Freeness values (cf. [11]).

V. CONCLUSIONS

In this study we have catalogued the two-phase properties of a library of suspensions of wood pulp. Conventionally, these properties are characterized by how the permeability and solid stress depend on the solid fraction. Pulp suspensions show very limited recovery on unloading, and so we interpret the rate-independent solid stress as a compressive plastic yield stress. Following previous work [15, 16, 27, 28, 32, 44], we have included a rate-dependent component to the solid stress with the form of a bulk viscosity to gauge whether this addition improves theoretical modelling of the dewatering behaviour of the entire pulp library. The library consisted of a range of different source woods and preparation and refinement techniques, which we split into three broad 'families': chemical pulps with variant degrees of chemical, but not mechanical, refinement; mechanically refined chemical pulps; and mechanical pulps (with or without subsequent mechanical refinement).

Network permeability displays a great variation across the pulp library, whereas the compressive yield stress does not. Despite the variability in the permeability, and its relatively low range of values in comparison to more idealized fibrous porous media, we have shown that a simple shift of the data can align the different pulps, both with one another and with a law proposed by Jackson & James for ideal fibres. This shift can be interpreted as a combination of scaling of the solid fraction, accounting for the fact that the fibre walls are themselves porous and inaccessibly trap water, and a scaling of the fibre dimensions, to account for the relatively complicated geometry of the pulp fibres which indicates that fibre radius may not be the typical pore scale. Indeed, we found that our pulp library naturally segregated into two distinct groupings, based on whether the pulp had undergone any form of mechanical treatment

or not, with the former appearing to reveal a distinct, lower, characteristic pore scale.

The main feature of the compressive yield stress of the pulps is that they uniformly follow a power law $P_y \sim \phi^2$ for low solid volume fraction ϕ. This is different from a plastic stress stemming from frictional rearrangements under elastic bending forces that apparently characterizes more ideal fibres like nylon. Instead, the $\phi-$dependence of the stress may be more consistent with frictional rearrangements under forces due to to local collapse or buckling of the fibre wall. Thus, pulp suspensions appear to follow a different microstructural paradigm.

The dewatering tests demonstrate definitively that the inclusion of a rate-dependent solid stress permits the two-phase model to better represent observations. This feature remains true for all the pulps in the library, with the main discrepancy between the model and experiments apparently due to the problematic loss of fines (small-scale debris generated by pulp production or refinement) during compaction. Interestingly, the bulk viscosity representation that we have adopted (and which works well) has the same power-law dependence on the solid fraction as the low$-\phi$ compressive yield stress, suggestive of a local viscous contact force, and is inversely related to the characteristic permeability scale, as expected if that pore scale also controls the viscous dissipation. Nevertheless, it is difficult to match the magnitude of the observed bulk viscosity using crude scaling theory, and the detailed origin of the rate dependent stress in pulp suspensions remains unclear and worthy of further investigation. Again, this behaviour contrasts with the dewatering behaviour of a nylon suspension, for which no solid bulk viscosity is apparent, reinforcing the different nature of the two-phase paradigm for pulp.

Many of the issues left open by the current work may be understood by performing dewatering experiments in conjunction with detailed imaging of the deforming solid network at the miscroscopic level. This exercise would inform the factors that control the permeability, the mechanics underscoring the compressive yield stress, and the origin of the bulk viscosity.

ACKNOWELEDGMENTS

Financial assistance from both Valmet and the Natural Sciences and Engineering Research Council of Canada, is gratefully acknowledged. We would also like to thank Dr Tomas Vikström and Mr Jean-Pierre Bousquet for many enlightening conversations throughout the course of this project.

[1] P. Pettersson, K. Lindgren, T. S. Lindstrom, and T. Wikstrom. Development of material models for dewatering of pulp suspensions. *The 19th International Symposium on Transport Phenomena, 17-20 August, 2008*, 2008.

[2] M. Kataja, K. Hiltunen, and J. Timonen. Flow of water and air in a compressible porous medium. a model of wet pressing of paper. *Journal of Physics D: Applied Physics*, 25:1053–1063, 1992.

[3] V. Lobosco, B. Norman, and S. Ostlund. Modelling of forming and densification of fibre mats in twin-wire formers. *Nordic Pulp and Paper Research Journal*, 20(1):16–23, 2005.

[4] J. C. Roux and J. P. Vincent. A proposed model in the analysis of wet pressing. *Tappi Journal*, 74(2):189–191, 1991.

[5] K. A. Jonsson and B. T. L. Jonsson. Fluid flow in compressible porous media: II: dynamic behaviour. *AIChE Journal*, 38(9):1349–1356, 1992.

[6] E. R. Ellis, W. H. Ceckler, E. V. Thompson, and J. F. Hoering. Computer model of a transversal flow press nip: predictions using experimentally determined permeability and compression data. *89th National AIChE Meeting, Portland 1980*, 1980.

[7] D. Bezanovic, C. J. van Duijn, and E. F. Kaasschieter. Analysis of paper pressing: the saturated one-dimensional case. *Journal of Applied Mathematics and Mechanics*, 86(1):18–36, 2006.

[8] D. M. Audet and A. C. Fowler. A mathematical model for compaction in sedimentary basins. *Geophysical Journal International*, 110:577–590, 1992.

[9] F. Concha and R. Bürger. A century of research in sedimentation and thickening. *KONA Powder and Particle Journal*, 20:38–70, 2002.

[10] G. W. Jackson and D. F. James. The permeability of fibrous porous media. *The Canadian Journal of Chemical Engineering*, 64:364–374, 1986.

[11] J. D. Lindsay and P. H. Brady. Studies of anisotropic permeability with applications to water removal in fibrous webs - Part 1. *Tappi Journal*, 76(9):119–127, 1993.

[12] J. D. Lindsay and P. H. Brady. Studies of anisotropic permeability with applications to water removal in fibrous webs - Part 2. *Tappi Journal*, 76(11):167–174, 1993.

[13] P. Pettersson, T. Wikstrom, and T. S. Lundstrom. Method for measuring permeability of pulp suspension at high basis weights. *Journal of Pulp and Paper Science*, 34:191–197, 2008.

[14] H. Vomhoff. On the in-plane permeability of water-saturated fibre webs. *Nordic Pulp and Paper Research Journal*, 15:200–210, 2000.

[15] D. R. Hewitt, D. T. Paterson, N. J. Balmforth, and D. M. Martinez. Dewatering of fibre suspensions by pressure filtration. *Physics of Fluids*, 28, 2016.

[16] R. Buscall and L. R. White. The consolidation of concentrated suspensions. Part 1. The theory of sedimentation. *Journal of the Chemical Society, Faraday Transactions 1: Physical Chemistry in Condensed Phases*, 83:873–891, 1987.

[17] K. A. Landman, C. Sirakoff, and L. R. White. Dewatering of flocculated suspensions by pressure filtration. *Physics of Fluids A: Fluid Dynamics (1989-1993)*, 3:1495–1509, 1991.

[18] R.G. de Kretser, D.V. Boger, and P.J. Scales. Compressive rheology: an overview. *Rheology Reviews*, pages 125–166, 2003.

[19] C. M. van Wyk. Note on the compressibility of wool. *Journal of the Textile Institute Transactions*, 37(12):T285–T292, 1946.

[20] S. Toll. Packing mechanics of fibre reinforcements. *Polymer Engineering and Science*, 38(8):1337–1350, 1998.

[21] C. P. J. Bennington, R. J. Kerekes, and J. R. Grace. The yield stress of fibre suspensions. *The Canadian Journal of Chemical Engineering*, 68:748– 757, 1990.

[22] R. L. Jones. *An investigation of the effect of fiber structural properties on the compression response of fibrous beds*. PhD thesis, Georgia Institute of Technology, 1962.

[23] J. sI. Dunlop. On the compression characteristics of fibre masses. *The Journal of The Textile Institute*, 74(2):92–97, 1983.

[24] D. T. Paterson. *Understanding the Dynamics of Pulp Fibre Suspension Dewatering*. University of British Columbia, 2020.

[25] H. Vomhoff and A. Schmidt. The steady-state compressibility of saturated fibre webs at low pressures. *Nordic Pulp and Paper Research Journal*, 12, 1997.

[26] V. Lobosco. *On the modelling of mechanical dewatering in papermaking*. PhD thesis, KTH Royal Institute of Technology, 2004.

[27] D. T. Paterson, T. S. Eaves, D. R. Hewitt, N. J. Balmforth, and D. M. Martinez. Flow-driven compaction of a fibrous porous medium. *Phys. Rev. Fluids*, 4:074306, 2019.

[28] M. Kvick, D. M. Martinez, D. R. Hewitt, and N. J. Balmforth. Imbibition with swelling: capillary rise in thin deformable porous media. *Physical Review Fluids*, 2(7):074001, 2017.

[29] B. Derakhshandeh, R. J. Kerekes, S. G. Hatzikiriakos, and C. P. J. Bennington. Rheology of pulp fibre suspensions: A critical review. *Chemical Engineering Science*, 66:3460–3470, 2011.

[30] R. J. Kerekes. Rheology of fibre suspensions in papermaking: An overview of recent research. *Nordic Pulp and Paper Research Journal*, 21(5):100–114, 2006.

[31] V. Lobosco and V. Kaul. An elastic/viscoplastic model of the fibre network stress in wet pressing: Part 1. *Nordic Pulp and Paper Research Journal*, 16(1):12–17, 2001.

[32] C. Holmqvist and A. Dahlkild. Consolidation of sheared, strongly flocculated suspensions. *American Institute of Chemical Engineers J.*, 54(4):924–939, 2008.

[33] D. A. Drew and S. L. Passman. *Theory of multicomponent fluids*, volume 135. Springer Science & Business Media, 2006.

[34] H. Nanko, A. Button, and D. Hillman. *The World of Market Pulp*. WOMP,LLC, Appleton, Wi., 2005.

[35] G. A. Smook. *Handbook for Pulp and Paper Technologists*. Angus Wilde Publications Inc., 2 edition, 1997.

[36] J. E. Stone and A. M. Scallan. The effect of component removal upon the porous structure of the cell wall of wood. ii. swelling in water and the fibre saturation point. *Tappi Journal*, 50(10):496–501, 2014.

[37] P. Lahtinen, S. Liukkonen, J. Pere, A. Sneck, and H. Kangas. A comparative study of fibrillated fibers from different mechanical and chemical pulps. *BioResources*, 9(2):2115–2127, 2014.

[38] K. Terzaghi. *Theoretical Soil Mechanics*. John Wiley and Sons, Inc., 1943.

[39] S. Bounoua, E. Lemaire, J. Férec, G. Ausias, A. Zubarev, and P. J. J. M. Kuzhir. Apparent yield stress in rigid fibre suspensions: the role of attractive colloidal interactions. *Journal of Fluid Mechanics*, 802:611–633, 2016.

[40] G. Carlsson, T. Lindstrom, and T. Floren. Permeability to water of compressed pulp fiber mats. *Svensk Papperstidning*, 86(12):R128–R134, 1983.

[41] J. D. Lindsay. The anisotropic permeability of paper. *Tappi Journal*, 73(5):223–229, 1990.

[42] W. L. Ingmanson. Internal pressure distribution in compressible mats under fluid stress. *TAPP1*, 42:840–849, 1959.

[43] S. Mueller, E. W. Llewellin, and H. M. Mader. The rheology of suspensions of solid particles. *Proceedings of the Royal Society A: Mathematical, Physical and Engineering Sciences*, 466(2116):1201–1228, 2010.

[44] T. S. Eaves, D. T. Paterson, D. R. Hewitt, N. J. Balmforth, and D. M. Martinez. Dewatering saturated, networked suspensions with a screw press. *Journal of Engineering Mathematics*, 120:1–28, 2020.

[45] L. Lundquist, F. Willi, Y. Leterrier, and J. A. E. Manson. Compression behavior of pulp fiber networks. *Polymer Engineering and Science*, 44(1):45–55, 2004.

[46] A. A. Roberston and S. G. Mason. Specific surface of cellulose fibres by the liquid permeability method. *Pulp and Paper Mag. Can.*, 50(13):103–110, 1949.

[47] J. D. Lindsay. Relative flow porosity in fibrous media: measurements and analysis, including dispersion effects. *Tappi Journal*, 77(6):225–239, 1994.

[48] G. V. Laivins and A. M. Scallan. Removal of water from pulps by pressing. *Tappi Journal*, 77(3):125–131, 1994.

[49] A. M. Scallan and J. E. Carles. The correlation of the water retention value with the fibre saturation point. *Svensk Papperstidning*, 75(17):699–703, 1972.

[50] C. T. J. Dodson. Fibre crowding, fibre contacts and fibre flocculation. *Tappi J*, 79(9):211–216, 1996.

[51] A. P. Philipse. The random contact equation and its implications for (colloidal) rods in packings, suspensions, and anisotropic powders. *Langmuir*, 12(5):1127–1133, 1996.

[52] C. Servais, J. A. E. Manson, and S. Toll. Fiber-fiber interaction in concentrated suspensions: Disperse fibers. *Journal of Rheology*, 43(4):991–1004, 1999.

[53] C. J. S. Petrie. The rheology of fibre suspensions. *Journal of Non-Newtonian Fluid Mechanics*, 87(2-3):369–402, 1999.

[54] M. Djalili-Moghaddam and S. Toll. A model for short-range interactions in fibre suspensions. *Journal of Non-Newtonian Fluid Mechanics*, 132:73–83, 2005.